Dynamic Adaptive Porous Cu Current Collector for Low N/P Ratio Li Metal Batteries

Jianyu Chen,[a] Wei Fu,[a] Shihao Zhang,[a] Fanlai Zhang,[a] Jiayi Zhou,[a] Yanwen Ma,*[a, b] and Jin Zhao*[a]

Porous copper (Cu) current collectors effectively suppress the growth of lithium (Li) dendrites and enhance the stability of Li metal anodes. However, the current development of porous Cu hosts generally involves a high proportion of Cu, mostly rigid structures, small pore volumes, and low Li utilization. Here, we propose a dynamic adaptive porous Cu (DAP–Cu) host, which is lightweight with a high pore volume, fabricated using a large aspect ratio of Cu nanowires as the building blocks. This DAP–Cu allows for the precise loading of metallic Li, and the symmetric battery assembled with Li/DAP–Cu electrode oper-

ates at the high current density of 5 mA cm^{-2} for 4000 hours while exhibiting a low polarization voltage of ~60 mV. The Li/DAP–Cu anode achieves high-performance compatibility with LiFePO$_4$ and sulfur cathodes, with optimal N/P ratios of 1.20:1 and 4.0:1, respectively. Full and pouch cells with low N/P ratios exhibit exceptionally high specific capacities and long-term cycling life. The establishment of standards for the matching of anodes and cathodes provides a reference for the quantitative preparation of electrode materials and is of significant guidance for enhancing the efficient utilization of metallic Li.

Introduction

Building a low-carbon, clean, and safe energy system with new energy as the core is vital for achieving carbon neutrality.[1] The transition hinges on enhancing the proportion and efficiency of renewable energy like solar and wind due to their intermittent nature require robust energy storage solutions to manage their output variability.[2] Among various storage options, electrochemical energy storage, particularly lithium (Li)-ion batteries (LIBs), stands out because of its configuration flexibility, rapid response, mass production ease, and scalability.[3] Despite LIBs' significant advancements in energy density, cycling life, and cost over the past 30 years, they cannot meet the rising energy demands of new power systems to support high renewable energy shares due to their approaching theoretical energy density limits.[4] Consequently, the surge in energy demands from electric vehicles to consumer electronics also presses the need for batteries with greater energy density, driving the exploration of new energy storage systems to transcend current limitations and support global carbon neutrality goals.[5]

Using metallic Li as the anode of Li metal batteries (LMBs) is recognized for their ultrahigh energy storage density, driven by Li's low density (0.534 g cm^{-3}), high theoretical gravimetric capacity (3860 mAh g^{-1}) and low electrochemical potential

(−3.04 V vs. SHE).[6] These characteristics make LMBs an excellent candidate for future high-energy-density battery systems. In recent years, studies have focused on assembling Li metal to match high-capacity sulfur (S) and oxygen (O$_2$) cathodes in Li–S and Li–O$_2$ battery systems, which offer enhanced specific and volumetric energy densities.[7] However, the practical application of LMBs is challenged by issues such as dendritic Li formation and inhomogeneous Li deposition at the anode.[8] Significant efforts have been directed toward regulating the deposition/dissolution behavior of metallic Li and developing anode stabilization techniques.[9] Advances in understanding dendrite formation and improving anode structure, interface, and electrolyte modifications have positioned LMBs as promising next-generation batteries with the potential for high commercial impact.[10]

Current theoretical models like the space charge, non-uniform nucleation, deposition-dissolution, and plating-stress-driven Li dendrite growth models provide insights into the nucleation and growth of Li dendrites.[11] Specifically, the space charge model highlights that dendrites form when Li-ion concentration drops to zero under high current densities at the electrode surface, suggesting that reducing effective current density or increasing the Li-ion migration rate can delay dendrite formation.[12] This underscores the importance of balancing Li-ion concentration and current density distribution on the electrode surface to suppress dendrite growth.[13] Additionally, the design of the current collector, particularly in anode structure, is crucial. In contrast, conventional planar current collectors like copper (Cu) foil (PL–Cu) struggle with uniform charge distribution and stress relief during deposition, while three-dimensional (3D) porous Cu hosts show marked improvements in managing these challenges, enhancing overall battery performance.[14]

In recent years, researchers have focused on developing new types of porous Cu hosts and stabilizing LMAs.[15] In 2015,

[a] Dr. J. Chen, W. Fu, S. Zhang, F. Zhang, J. Zhou, Prof. Y. Ma, Prof. J. Zhao
State Key Laboratory of Organic Electronics and Information Displays & Institute of Advanced Materials (IAM), Nanjing University of Posts & Telecommunications, 9 Wenyuan Road, Nanjing 210023, China
E-mail: iamywma@njupt.edu.cn
       iamjzhao@njupt.edu.cn

[b] Prof. Y. Ma
Suzhou Vocational Institute of Industrial Technology, 1 Zhineng Avenue, Suzhou International Education Park, Suzhou 215104, China

Supporting information for this article is available on the WWW under https://doi.org/10.1002/batt.202400304

Guo's group pioneered the stabilization of LMAs using a 3D Cu host fabricated through an electrochemical approach on PL–Cu, which helped understand how the increased electroactive surface area could suppress dendrite growth.[16] Similarly, Wang et al. utilized laser technology to create a porous Cu host, analyzing the impact of pore size, depth, and spacing on electrochemical performance through finite element simulation (FEA).[17] Although these innovations have suppressed Li dendrite growth and enhanced anode stability, challenges such as low porosity and limited Li loading capacity still exist.[18] Addressing these issues, Chen et al. have proposed strategies like dynamic, intelligent porous Cu hosts, which use Cu microparticles with adjustable junctions to increase spacing during Li deposition, enhancing Li loading accommodation and paving the way for advancing Li metal batteries with high energy densities.[19]

Previous research on LMBs, such as Li–lithium iron phosphate (Li–LiFePO$_4$), Li–S, and Li–O$_2$ types, often relied on using Li foil with excess metallic Li at the anode to mitigate the impact of metallic Li loss on cathode performance, which constrained improvements in battery energy density.[20] Therefore, to enhance battery electrochemical performance and energy density, it is crucial not only to increase the loading of metallic Li in composite anodes to match with high-capacity cathode materials but also to improve the utilization efficiency of metallic Li in LMBs.[21]
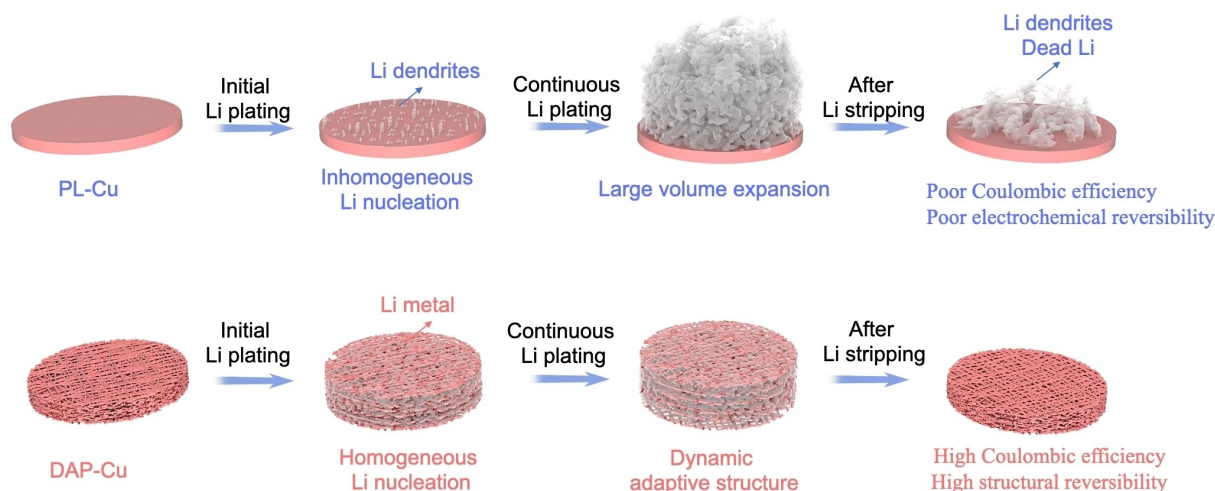
Herein, we developed a dynamic adaptive porous Cu network current collector (DAP–Cu) using self-assembled Cu nanowires, which form a 3D conductive network enhancing the battery's rate performance. The high aspect ratio and flexibility of this network dynamically adjust to the metallic Li's deposition and dissolution processes by expanding and contracting, thus maintaining dendrite-free growth even when the deposited Li (8 mAh cm^{-2}) exceeds the maximum theoretical Li loading capacity of DAP–Cu (5.8 mAh cm^{-2}). Utilizing composite anodes with quantitatively loaded Li and pairing with LiFePO$_4$ and S cathodes, batteries tested at different N/P ratios showed that Li–LiFePO$_4$ and Li–S batteries matched the cycling capacities of full cells assembled with Li foil at N/P ratios of 1.20∶1 and 4.0∶1, respectively. These configurations demonstrated high metallic Li utilization, excellent rate performance, and extended cycling life, especially notable in Li/DAP–Cu∣LiFePO$_4$-based pouch cells, which exhibited high reversible capacity and prolonged Coulombic efficiency.

Results and Discussion

The behavior of Li metal deposition/dissolution on PL–Cu and DAP–Cu electrodes is depicted in Scheme 1. The surface of the PL–Cu is characterized by a large number of irregular protrusions that create a disordered distribution of charge and cannot regulate a uniform Li-ion flux, resulting in heterogeneous nucleation sites. Additionally, the PL–Cu cannot buffer the volume changes associated with the expansion and contraction of metallic Li, leading to uncontrolled expansion, uneven Li deposition, and dendritic growth. The residual dendritic Li and "dead Li" on the electrode surface after reversible charging and discharging cycles decrease the Coulombic efficiency of the battery and can introduce safety risks. The DAP–Cu electrode, using high-aspect-ratio Cu nanowires (Cu NWs) as the building blocks, exploits the high flexibility and conductivity of metal nanowires to create a network with substantial porosity and conductivity. This configuration significantly reduces the nucleation overpotential on the electrode surface and ensures a uniform Li-ion flux. The interconnected nanowire-to-nanowire structure provides numerous nucleation sites that facilitate the initial formation of metallic Li. Moreover, the flexible network of metal nanowires can adapt the distance between the nanowires to accommodate the considerable volume expansion of metallic Li, effectively releasing the internal stress generated from the Li deposition process and mitigating the volume changes caused by the repeated Li deposition/dissolution.

The DAP–Cu host uses a high-aspect-ratio Cu NWs as the fundamental building block. Freshly synthesized Cu NWs (Fig-

Scheme 1. Schematic illustration of Li deposition/dissolution behavior on PL–Cu and DAP–Cu host.

ure S1), after being vacuum-filtered and dried, undergo a reductive atmosphere annealing treatment to obtain the final DAP–Cu host. As shown in Figure 1a and **1b**, the diameter of the Cu NWs is approximately 50 nm. The DAP–Cu film, formed by solvent evaporation, is loosely porous with a thickness of ~100 μm. The pristine Cu NWs are easily oxide in the air (Figure S2), and the resistance of Cu NWs before and after annealing treatment is tested using a Four-Probe method. The sheet resistance of reduced Cu NWs is approximately 10 mΩ sq^{-1}, indicating that the DAP–Cu host possesses good conductivity (Figure S3). As shown in Figure 1c and **1d**, it is evident that the nanowires in DAP–Cu interlink to form a network structure, which is a major reason for the high electrical conductivity of the DAP–Cu electrodes. Additionally, the DAP–Cu host exhibits excellent flexibility and maintains the film's integrity even when bent to any degree (Figure 1e). Figure 1f shows that the DAP–Cu electrode can be cut to any desired shape, making it suitable for the preparation requirements of different types of batteries. XRD analysis indicates that the original oxidized Cu NWs are effectively reduced under a reductive atmosphere at 200 °C for 0.5 hours (Figure 1g). Mercury intrusion porosimetry reveals the pore volume and pore size distribution of the DAP–Cu current collector, the

100 μm thick DAP–Cu (DAP–Cu-100) has an average pore volume of 0.208 cm^3 g^{-1} and an average pore diameter of 1 μm (Figure 1h and **1i**). DAP–Cu current collectors with different thicknesses exhibit consistent cumulative pore volumes and similar pore diameters, demonstrating the reproducibility of this DAP–Cu current collector constructed from Cu NWs (Figure S4). To investigate the effect of electrode structure on the nucleation and deposition behavior of Li metal, finite element analysis (FEA) was used to study the relationship of structural design to the current density distribution, electrolyte concentration distribution, and growth morphology of metallic Li. According to the simulation results, as shown in the Figure S5, the current density on the DAP–Cu electrode surface exhibits a more uniform distribution compared to the PL–Cu surface. Additionally, the DAP–Cu electrode has a more uniform Li ion flux density than the PL–Cu electrode, which can enhance the contact between the electrode surface and Li ions and then accelerate the transport of Li ions (Figure S6). Furthermore, Figure S7 shows simulations of the Li metal plating process on PL–Cu and DAP–Cu electrodes. Metallic Li presents stable and uniform deposition trend on the DAP–Cu structure. In contrast, for the PL–Cu electrode, metallic Li grows in the form of disordered Li dendrites.
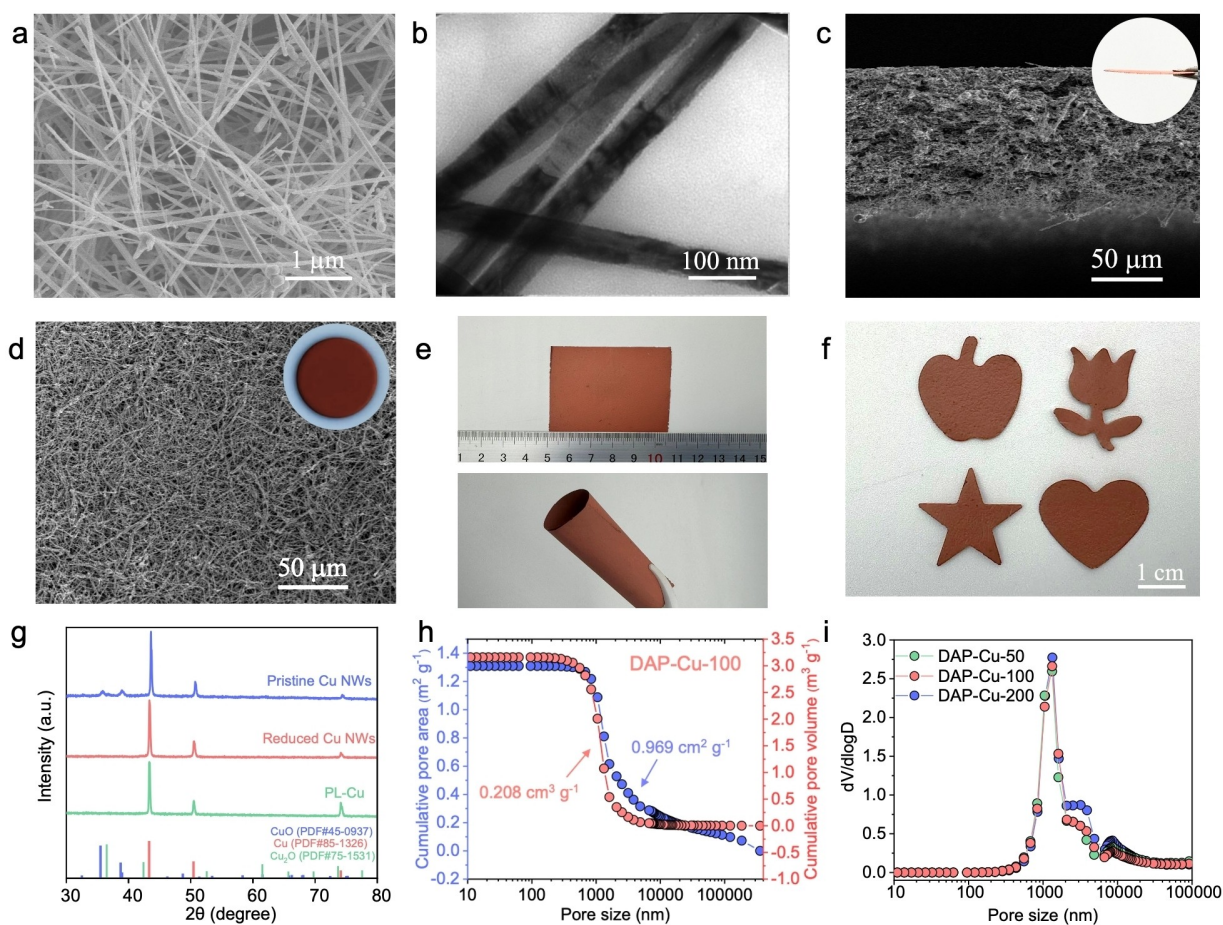

Figure 1. Morphological and structural characterizations of DAP–Cu host. (a) SEM image of the high-aspect-ratio Cu NWs, (b) TEM image of the high-aspect-ratio Cu NWs, (c) cross-sectional SEM image of DAP–Cu host, (d) top-view SEM image of DAP–Cu host, (e) digital photo of the large-area flexible DAP–Cu host, (f) digital photo of the DAP–Cu host with four different shapes, (g) XRD patterns of pristine Cu NWs, reduced Cu NWs, and pure PL–Cu, (h) cumulative pore volume and cumulative pore area of DAP–Cu host, (i) pore size distribution of DAP–Cu host.

Batteries & Supercaps

Research Article
doi.org/10.1002/batt.202400304

Chemistry
Europe

European Chemical
Societies Publishing

Metallic Li could be filled in the generated pores of DAP–Cu. Thus, the maximum Li loading of DAP–Cu depends on the porosity of the DAP–Cu structure. To observe the structural changes in DAP–Cu with Li deposition, half-cells were assembled for depositing Li at varying capacities. As shown in Figure 2a and **2b**, with a small increase of Li (1 mAh cm^{-2}), the Li uniformly fills the interior of the DAP–Cu structure. When the deposition amount increases to 4 mAh cm^{-2}, the side-view SEM of DAP–Cu shows Li uniformly filled within the host due to DAP–Cu's porosity allowing for ~5.8 mAh cm^{-2} of Li, thereby exhibiting a dendrite-free morphology. Interestingly, when the Li deposition amount increases to 8 mAh cm^{-2}, a value far exceeding the static pore volume limit of DAP–Cu, The Li still uniformly fills DAP–Cu without overflowing the surface of the DAP–Cu electrode. This indicates that DAP–Cu likely undergoes some dynamic volume changes to accommodate the volume expansion of Li. To verify the dynamic expansibility of the DAP–Cu host formed by the stacked nanowire structure, an optical setup was used for in-situ real-time observation of structural changes in the DAP–Cu. As shown in Figure 2c, at 10 mA cm^{-2} current density and after depositing for 15 minutes, Li initially prefers to deposit inside the Cu NWs stacked structure. Subsequently, the Li begins to expand throughout the entire Cu NWs framework. As time increases to 30 minutes, Li gradually fills the interior of the NWs network, then starts to extend outward, causing the DAP–Cu to be significantly expanded. During constant charging process, Li is continuously removed from the DAP–Cu, maintaining the original morphol-

ogy and thickness. Indicating that the as-prepared current collector structure composed of a Cu NWs network is elastically adjustable. Initially, as Li begins to deposit, the larger charge density accumulated at the contact points between the Cu NWs induces preferential Li deposition at these sites. As the Li deposition increases, Li tends to deposit on already deposited Li. When the deposition amount reaches the limit that the original static stack can accommodate, the Cu NWs are expanded to accommodate more Li deposition. In contrast, observing the structural changes in PL–Cu current collector during Li deposition (Figure 2d), it can be seen that from the 30 minute, "hotspots" randomly appear on PL–Cu surface, where protruding Li induces preferential massive deposition in its area. After 60 minutes, numerous Li dendrites form, and even after dissolution testing, the dendritic structures on the surface remain (Figure S8). These results prove the advantages of the DAP–Cu structure in mitigating the formation and growth of Li dendrites.

The deposition/dissolution efficiency of metallic Li in the DAP–Cu host was tested in half-cells. As shown in Figure 3a and **3c**, the Coulombic efficiency of Li deposition/dissolution in PL–Cu and DAP–Cu hosts was evaluated under a current density of 1 mA cm^{-2} (Figure S9). The initial Coulombic efficiency of the DAP–Cu host was 93%, and this remained largely unchanged after 100 cycles, indicating high reversibility of Li deposition/dissolution in the DAP–Cu host. In contrast, the initial Coulombic efficiency for PL–Cu was 70%, and it began to show unstable fluctuations after 80 cycles. When increasing the current density to 5 mA cm^{-2}, the initial efficiency of Li deposition/dissolution in DAP–Cu remained high at 91% (Figure 3b and Figure S10). Comparing the long-term cycling CEs of both current collectors, it was evident that at higher current densities, DAP–Cu maintained high Coulombic efficiency and excellent cycling stability, whereas PL–Cu showed a trend of decreasing efficiency after the 20th cycle, suggesting that the uneven charge density distribution on the PL–Cu surface led to uneven deposition and dissolution behavior, leading to the generation of dendritic or "dead" Li. Furthermore, comparing the initial nucleation overpotentials of the two hosts, it was found that DAP–Cu has a smaller overpotential. This is attributed to the network structure formed by the Cu NWs, which has a large specific surface area, good electrolyte wettability, and excellent electric conductivity, thereby reducing interface impedance and minimizing polarization.

To compare the electrochemical stability of Li/DAP–Cu and Li/PL–Cu composite anodes, symmetric-cell tests were conducted under conditions of low and high current densities. Figure 3d shows a long-term cycling comparison of Li/DAP–Cu and Li/PL–Cu composite anodes at 1 mA cm^{-2} with 1 mAh cm^{-2}. The voltage-time curve of the symmetric cell with the Li/DAP–Cu composite anode remained stable even after 4000 hours, whereas the voltage curve of the Li/PL–Cu composite anode began to show increased polarization after only 400 hours (Figure S11). It was observed that the overpotential of DAP–Cu (~22 mV) was significantly lower than the PL–Cu-based electrode (~56 mV). When controlling Li deposition/dissolution to 1 mAh cm^{-2} and the current density to
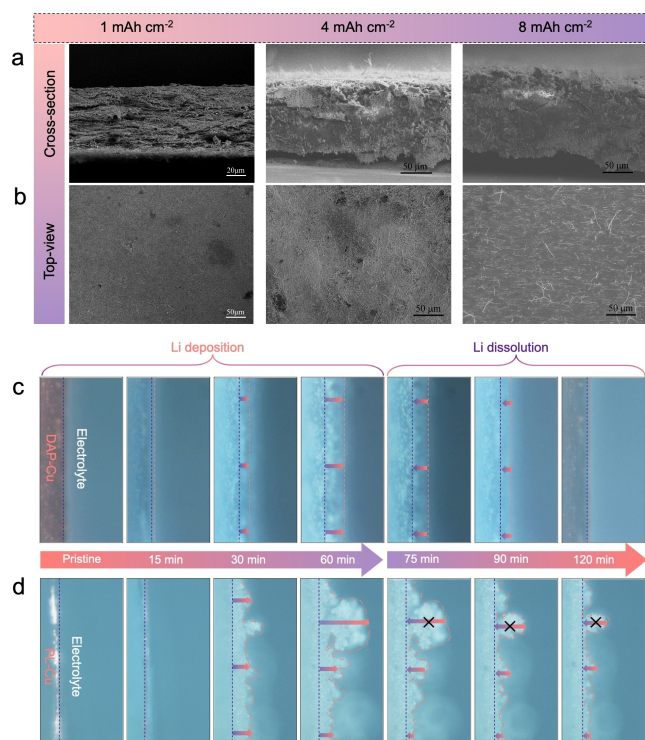

Figure 2. (a) side-view SEM images of Li deposition on DAP–Cu with an areal capacity of 1, 4 and 8 mAh cm^{-2}, (b) top-view SEM images of the Li plating on DAP–Cu with an areal capacity of 1, 4 and 8 mAh cm^{-2}, Dynamic electrochemical behavior of Li deposition/dissolution in DAP–Cu (c) and PL–Cu (d) captured by in-situ optical electron microscopy.
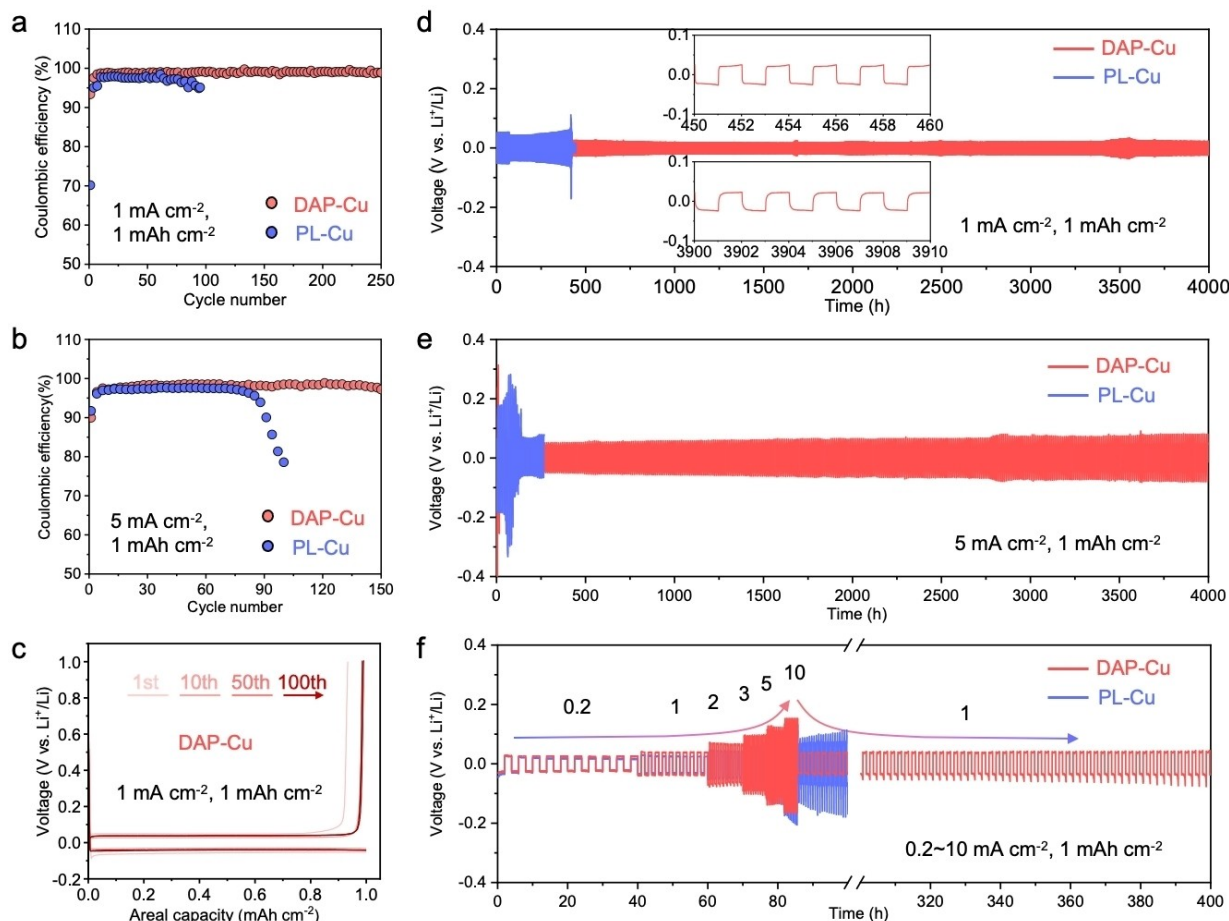
Figure 3. Electrochemical performance evaluation of DAP–Cu and PL–Cu host. Coulombic efficiency plots of DAP–Cu and PL–Cu host under the current density of (a) 1 mA cm^{-2} and (b) 5 mA cm^{-2} with a cycling capacity of 1 mAh cm^{-2}, (c) Charge/discharge voltage profiles of DAP–Cu host under 1 mA cm^{-2} current density and 1 mAh cm^{-2} cycling capacity, (d) voltage-time profiles of Li/DAP–Cu and Li/PL–Cu-based symmetric cells at t 1 mA cm^{-2} and 1 mAh cm^{-2}, (e) voltage-time profiles of Li/DAP–Cu and Li/PL–Cu-based symmetric cells at 5 mA cm^{-2} and 1 mAh cm^{-2}, (f) voltage-time profiles of L Li/DAP–Cu and Li/PL–Cu symmetric cells under various current densities with a fixed cycling capacity of 1 mAh cm^{-2}.

5 mA cm^{-2}, the voltage curve of the Li/DAP–Cu composite anode symmetric cell remained stable, with a maximum overpotential of ~60 mV. In contrast, the Li/PL–Cu composite anode showed a higher instability within 300 hours, leading to a short circuit (Figure 3e). As shown in Figure 3f, when the charge/discharge capacity is fixed and the current densities vary from 0.2 to 5 mA cm^{-2}, low overpotentials from ~20 mV (0.2 mA cm^{-2}) to ~100 mV (5 mA cm^{-2}) was obtained. Even at 10 mA cm^{-2} and a Li deposition/dissolution capacity of 1 mAh cm^{-2}, the polarization curves in each cycle of 10 cycles remain stable. On the other hand, the charge/discharge curves of the Li/PL–Cu battery showed significant fluctuations and short-circuited after 50 cycles. These fluctuations originated from uneven deposition and rampant growth of dendritic Li, piercing the separator and inducing the direct contact from the anode to the cathode. Meanwhile, the DAP–Cu host can regulate homogeneous deposition/dissolution of Li and effectively suppress the growth of Li dendrites.

Compared to full cells using Li foil as the anode, introducing a 3D porous current collector in Li composite anodes can improve the utilization rate of Li. Therefore, full cells were

constructed using different cathode-to-anode capacity (N/P) ratios to test the initial charge/discharge capacities and to study the optimal matching relationship between cathode and anode. Initially, the mass of the cathode (LiFePO$_4$) was fixed at 6.4 mg cm^{-2} which corresponding to the areal capacity of 1 mAh cm^{-2}, and the anode was quantitatively loaded with metallic Li to achieve the corresponding capacity. Both types of full cells used Li foil (excess Li) as a control in the cell tests. As shown in Figure 4a, when the N/P ratio was 0.5:1, the initial discharge capacity of the LiFePO$_4$-based full cell was only 50 mAh g^{-1}. As the capacity of the Li anode increased, the initial charge/discharge capacity also increased and reached the same level as that of the full cell assembled with Li foil at a low N/P ratio of 1.2:1. This demonstrated that the maximum efficiency of Li utilization could be achieved only when the capacity of the anode Li exceeded the cathode by 0.2 times, with the utilization efficiency of metallic Li being 83.3% (Figure 4b). Long-term cycling tests were conducted on the full cell with an N/P ratio of 1.2:1. At a 1 C rate, the Li/DAP–Cu electrode assembled full cell exhibited stable Coulombic efficiency and
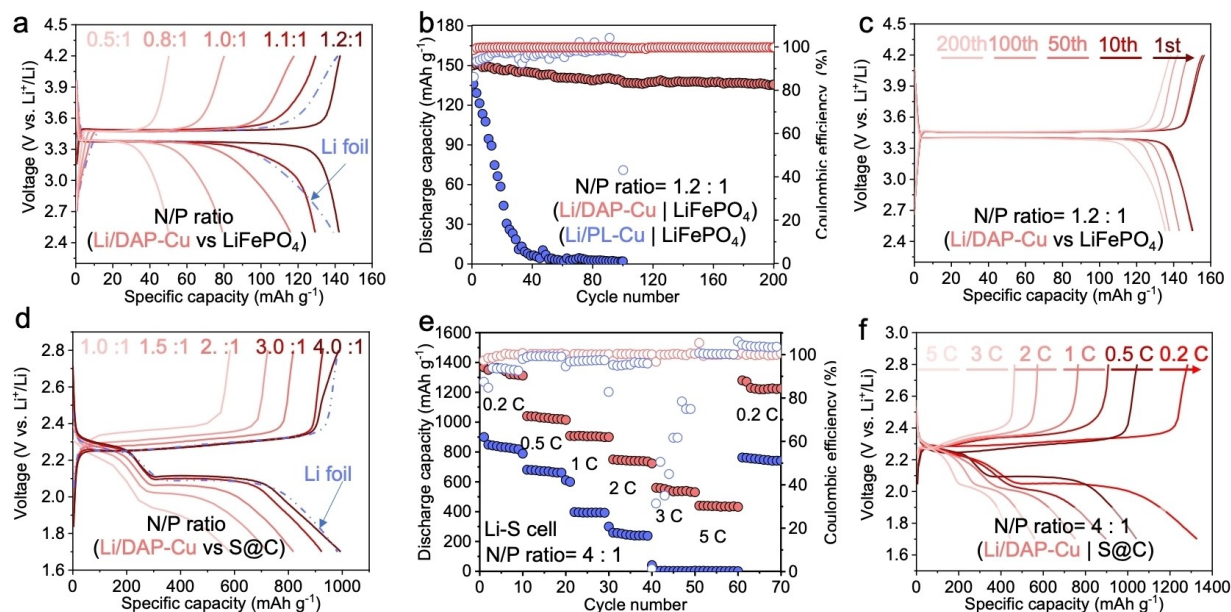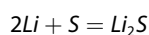
Batteries & Supercaps

Research Article
doi.org/10.1002/batt.202400304

Chemistry
Europe
European Chemical
Societies Publishing

Figure 4. Electrochemical performance of LFP cathode-based and S cathode-based full cells. (a) Full cell discharge/charge curves at a 1 C rate with N/P ratios of 0.5:1, 0.8:1, 1.0:1, 1.1:1, and 1.2:1 compared with Li foil|LiFePO$_4$ full cells, (b) long-term cycle stability at a 1 C rate for a Li/DAP–Cu|LiFePO$_4$ full cell with an N/P ratio of 1.2:1 and a Li foil|LiFePO$_4$ full cell, (c) discharge/charge curves of at different rates for a Li/DAP–Cu|LiFePO$_4$ full cell with an N/P ratio of 1.2:1 and a Li foil|LiFePO$_4$ full cell, (d) discharge/charge curves of Li–S full cell at a 1 C r with N/P ratios of 1.0:1, 1.5:1, 2.0:1, 3.0:1, and 4.0:1 compared with Li foil|S full cells, (e) long-term cycle stability at a 1 C rate for a Li/DAP–Cu|S full cell with an N/P ratio of 4.0:1 and a Li foil|S full cell, (f) discharge/charge curves of at different rates for a Li/DAP–Cu|S full cell with an N/P ratio of 4.0:1 and a Li foil|S full cell.

high capacity retention (Figure 4c), whereas the Li/PL–Cu|LiFePO$_4$ cell showed rapid capacity decay (Figure S12).

Compared to LiFePO$_4$ full cells, Li–S batteries rely more on the high utilization rate of Li. Studying the capacity-matching relationship between cathode and anode materials in Li–S batteries is significant to their development. In this study, the cathode of the Li–S battery consisted of S-loaded porous carbon (S@C), with the loading of S on the cathode (1 mg cm^{-2}), corresponding to an areal capacity of 1.67 mAh cm^{-2}. Full cells assembled with different Li loadings on Li/DAP–Cu and S@C were tested for their electrochemical performance. As shown in Figure 4d, as Li loading amount in the anode increased, the initial charge/discharge capacity of the Li/DAP–Cu|S@C full cell showed an increasing trend. When the cathode-to-anode matching ratio was 4.0:1, the initial charge/discharge capacity of the cell reached the same level of the full cell which assembled with Li foil. The reaction equation for Li–S batteries is

$$2Li + S = Li_2S$$

Ideally, 1 mol of S consumes 2 mol of Li in the reaction. In practical terms, when the N/P ratio is 2.0:1, the initial reversible capacity of the battery is ~852 mAh g^{-1}, partly because some of the Li participates in the formation of the SEI layer at the surface of the anode. Additionally, due to the complex reaction processes in Li–S batteries and the limited ability of the cathode to inhibit polysulfides, lower-order sulfides permeate the separator and migrate to the anode surface, reducing Li utilization efficiency. When the anode's Li capacity is twice that

of the cathode, the initial charge/discharge capacity is consistent with that of a Li–S battery assembled with Li foil. To further validate that an N/P ratio of 4.0:1 is the optimal matching value for the capacities of the cathode and anode in Li–S batteries, long-term cycling tests were conducted against full cells assembled with Li/PL–Cu. As shown in Figure 4e, under different current densities, the Li/DAP–Cu|S@C full cell exhibited higher discharge capacity and cycling stability. At a 5 C rate, the discharge capacity of the Li/DAP–Cu|S@C full cell remained at 817 mAh g^{-1} (Figure 4f). Notably, the capacity decay of Li/DAP–Cu|S C cells at high current densities is often attributed to the polysulfide shuttle effect in Li–S batteries. This shuttle effect occurs when lithium polysulfides, which are intermediate products formed during the discharge process, dissolve into the electrolyte and migrate between the anode and the cathode.[7g] In contrast, the discharge capacity of the Li/PL–Cu|S@C full cell showed significant decay, dropping from an initial discharge capacity of 954 mAh g^{-1} to 677 mAh g^{-1} (Figure S13). The results indicate that at an N/P ratio of 4.0:1, the Li/DAP–Cu|S@C battery exhibits high cycling stability.

DAP–Cu exhibit excellent mechanical flexibility and high conductivity, making them suitable as electrode materials for flexible Li metal batteries. Li/DAP–Cu anode and LiFePO$_4$ cathode were assembled into a pouch cell to test their electrochemical performance under various bending conditions. As shown in Figure 5a, the structure of the pouch cell is illustrated. Figure 5b displays a side-view SEM image of the layer structure of the pouch cell. Figure 5c shows the long-term cycling performance test of the pouch cell, where the initial discharge capacity reached 139.6 mAh g^{-1}, closely matching the
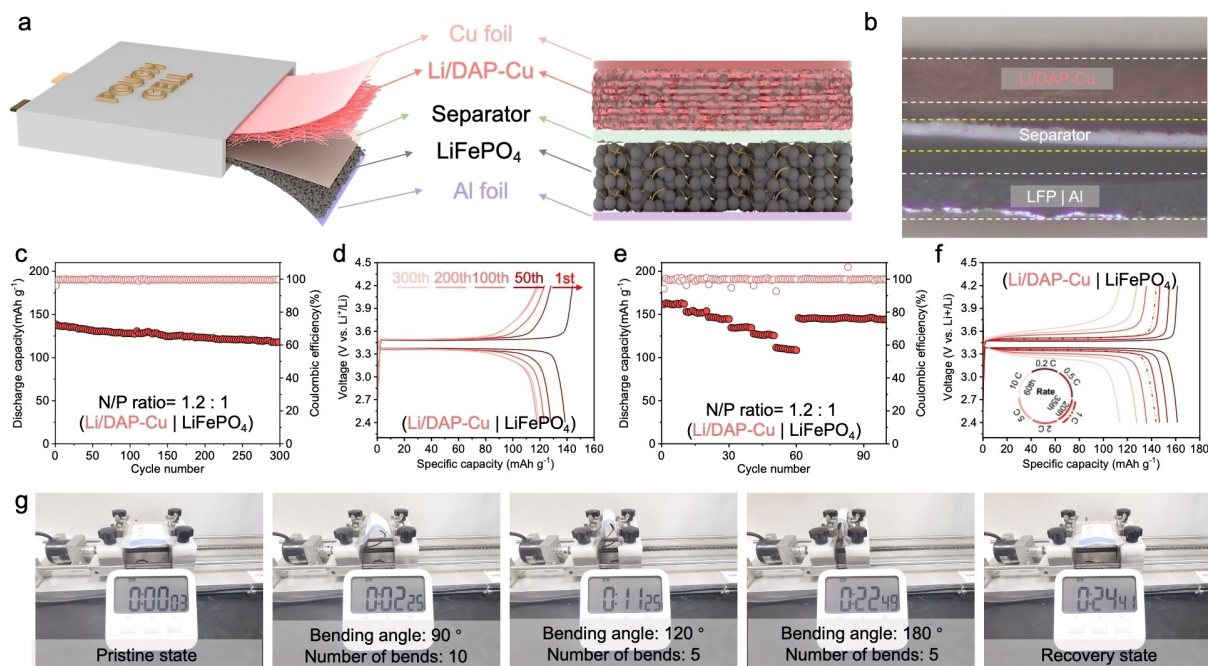
Figure 5. Electrochemical performance of LFP cathode-based pouch cell. (a) Schematic diagram of pouch cell structure, (b) side-view SEM image of the microstructure of the Li/DAP–Cu-based pouch cell, (c) long-term electrochemical performance of the Li/DAP–Cu-based pouch cell at a current density of 1 C, (d) charge/discharge curves of the Li/DAP–Cu-based pouch cell under 1 C, (e) cycling performance of the Li/DAP–Cu-based pouch cell under various rate conditions, (f) Charge-discharge curves of the Li/DAP–Cu-based pouch cell under various rate conditions, (g) digital photographs of the timer lit under different bending states of the Li/DAP–Cu-based pouch cell.

performance level of a coin cell. After 50 cycles, the discharge capacity decayed to 128.2 mAh g^{-1} and then remained stable through subsequent cycling. Figure 5d presents the charge/discharge curves of the pouch cell at the 1st, 50th, 100th, 200th, and 300th cycles, all exhibiting clear charge and discharge plateaus characteristic of LiFePO$_4$-based batteries. Figure 5e and **5f** display the electrochemical performance of the Li/DAP–Cu|LiFePO$_4$ pouch cell under various rates, showing high discharge capacity and electrochemical reversibility. As a result, a pouch cell device was made to light up a timer using the Li/DAP–Cu|LiFePO$_4$ pouch cell after 300 cycles. As shown in Figure 5g, under both unfolded and bent conditions, the Li/DAP–Cu|LiFePO$_4$-based pouch cell successfully power up the timer with nearly no visible change. These results demonstrate that the Li/DAP–Cu|LiFePO$_4$-based pouch cell can exploit the high Li utilization rate and excellent electrochemical performance. This indicates that the Li/DAP–Cu|LiFePO$_4$-based pouch cell possesses high flexibility, making it a promising candidate for flexible energy storage applications.

Conclusions

In summary, a dynamic adaptive porous Cu network host has successfully stabilized the Li metal composite anode. This study not only achieves large-scale preparation of composite anodes but also provides a foundation for applying metallic Li in high-energy-density batteries. By utilizing a DAP–Cu current collector to host Li in the composite anode, the capacity matching between the anode and cathode in the Li|LiFePO$_4$ and Li–S full battery systems was optimized. It was found that the optimal N/P ratio in the Li|LiFePO$_4$ full battery is 1.2:1, while in the Li–S full battery, the optimal N/P ratio is 4.0:1. Based on the Li/DAP–Cu electrode, half cells, symmetrical cells, and full cells all demonstrated excellent electrochemical performance, confirming its potential in the practical development of Li metal batteries. Additionally, the flexible pouch battery assembled with Li/DAP–Cu anode also showed high flexibility and excellent cycling stability, highlighting its potential applications in flexible energy storage devices.

Experimental Section

Materials

Copper nitrate (AR, purity $\geq$ 99.99%), sodium hydroxide (AR, purity $\geq$ 99.99%) and hydrazine hydrate (AR, 85 wt%) were purchased from Sinopharm Group Co., Ltd. 1,3 Propylenediamine was purchased from Aladin Reagent Company. Lithium iron phosphate (LFP), polyvinylidene fluoride (PVDF) powder, N–methylpyrrolidone (NMP), Super P and Li foil were purchased from Suzhou Duoduo Chemical Technology Co., Ltd. All chemicals were used directly without further purification.

Preparation of Cu NWs

A 120 g sample of sodium hydroxide was placed in a reaction flask, dissolved in ultrapure water up to 200 mL, and stirred until homogeneous solution generation (15 M). Next, 3 mL of a 1,3-

diaminopropane solution was injected into the sodium hydroxide solution via a syringe to obtain mixed solution **A**. A precursor, 2.4 g of copper(II) nitrate, was dissolved in 10 mL of ultrapure water to prepare a copper(II) nitrate ($Cu(NO_3)_2$) solution, which was then injected into mixed solution **A** via a syringe and stirred for 10 minutes to yield a uniformly mixed solution **B**. Subsequently, 100 μL of a hydrazine hydrate solution (35 wt%) was injected into mixed solution **B** and stirred for 30 minutes to form mixed solution **C**. This mixture was then left to stand in an ice–water bath for 1 hour before transferring to a water bath, where the reaction temperature was set at 60 °C for a duration of 1 hour. The upper layer of the reaction product was washed five times with ultrapure water and ethanol to obtain the Cu NWs samples, which were then vacuum-dried to collect the Cu NWs powder samples.

Preparation of DAP–Cu Current Collector

1 g of the aforementioned Cu NWs powder was dispersed in ethanol to create a Cu NWs dispersion. This dispersion was then subjected to vacuum filtration to obtain a wet, cake-like film, which was placed in a vacuum oven and heated (100 °C) to evaporate any residual solvent. During the evaporation process, the Cu NWs self-assembled to form a dry cake-like film. The dried nanowire samples are placed in a hydrogen–argon mixed atmosphere and heated at a rate of 5 °C/min to 200 °C. After maintaining this temperature for 2 hours, the samples are allowed to cool in the furnace. This process reduces the oxide layer on the nanowire surface. The nanowire samples are then cut into 12 mm diameter discs electrode, resulting in the DAP–Cu current collectors.

Preparation of Li/DAP–Cu

The Li/DAP–Cu composite anode was obtained using a constant current electrochemical deposition method. Using the DAP–Cu electrode as the cathode and Li foil as the anode, a coin cell was assembled. Cu foil was also used as a control in the experiment. The Li/DAP–Cu composite anode was fabricated by depositing Li at a current density of 1 mA cm^{-2}, aiming for a Li deposition amount of 1–10 mAh cm^{-2}.

Characterization

Scanning Electron Microscopy (SEM): 1 g of Cu NWs powder was dispersed in 100 mL of ethanol to prepare a 10 mg mL^{-1} Cu NWs dispersion. 50 μL of this dispersion was dropped onto a silicon wafer and vacuum-dried. The dried silicon wafer sample was then uniformly coated on conductive adhesive and fixed on the SEM sample stage. The sample's morphology was observed using a Hitachi S4800 SEM. The morphology of the Li/Cu composite anode was observed using ex-situ SEM; this required disassembling the battery inside an Ar-filled glove box, washing the electrode in DOL/DME solvent to remove residual electrolyte and LiTFSI salts, and drying to prepare the electrode for observation.

Transmission Electron Microscopy (TEM): 20 μL of the Cu NWs dispersion was dropped onto a Cu grid supported by a carbon film and evaporated. The morphology and structure of the sample were observed using a Hitachi S7700 transmission electron microscope.

Thin Film Resistivity Test: The sheet resistance was tested using a Four-Probe method on a Keithley 2400 source meter. In situ optical microscopy (YUESCOPE, YM710TR) was conducted to capture the Li plating/stripping behavior on DAP-Cu and PL-Cu current collectors.

Electrochemical Measurement

Half-cell testing involves using DAP–Cu or PL–Cu current collectors as the cathode and Li foil as the anode. For half-cell tests of blank electrodes, the cells are electro-activated between 0.1 to 1 V before electrochemical deposition and dissolution. A fixed amount of Li is deposited on the working electrode and stripped back to 1 V under specific current density conditions. Specifically, DAP–Cu electrodes and blank electrodes are assembled, firstly electrochemically depositing 1 mAh cm^{-2}, then the half-cell is charged to 1 V to ensure complete dissolution of Li in the composite anode. Repeated deposition/dissolution tests are conducted to determine Coulombic efficiency. Similarly, 1 mAh cm^{-2} is deposited on PL–Cu current collectors, followed by charging to dissolve Li, and then repeated charge/discharge cycles are performed to test Coulombic efficiency.

Symmetric cell testing is conducted for electrodes undergoing electrochemical Li plating in half-cells. Li is deposited at a current density of 1 mA cm^{-2} to an areal capacity of 2 mAh cm^{-2} on DAP–Cu or PL–Cu blank current collectors, then reassembled on the same electrode in the cell. The cells are cycled under specific experimental conditions to evaluate the battery's overpotential and cycling life.

N/P ratio of LiFePO$_4$ full cell testing involves preparing standardized cathodes by mixing LiFePO$_4$ powder, conductive carbon black, and polyvinylidene fluoride (PVDF) in an 8:1:1 mass ratio in N—methyl-2-pyrrolidone (NMP) solution, followed by vigorous stirring to form a slurry. The prepared slurry is coated on carbon-coated Al foil, dried in an air oven for 1 hour, and then transferred to a vacuum oven for 12 hours. The prepared LiFePO$_4$ electrodes are cut into disc-liked eletrode with a diameter of 12 mm. The loading areal mass of LiFePO$_4$ is ~6.4 mg cm^{-2}, corresponding to a specific capacity of 1 mAh cm^{-2}. LiFePO$_4$ is assembled as the cathode in a full cell with Li foil as the anode. After the cell is left to rest for 1 hour and charged to 4.2 V to fully delithiate the LiFePO$_4$ (forming FePO$_4$), the delithiated FePO$_4$ electrode is removed for further use. Cells with different specific capacities of Li/DAP–Cu as the anode and FePO$_4$ as the cathode are assembled to test the first cycle charge/discharge curves and Coulombic efficiencies at different N/P ratios. The initial charge-discharge specific capacities of full cells at different N/P ratios are collected and compared to select the optimal N/P ratio parameters.

N/P ratio of Li—S full cell testing follows a similar procedure, using S@C powder mixed with conductive carbon black and PVDF in an 8:1:1 mass ratio in NMP solution to form a slurry. The as-prepared slurry is coated on carbon-coated Al foil, dried, and then cycled. Cells are assembled with varying capacities of Li/DAP–Cu as the anode and S@C as the cathode to test for optimal parameters through charge-discharge cycling and Coulombic efficiency.

The pouch cell includes a single Li/DAP–Cu electrode, Cu foil, LFP cathode, separator, electrolyte, and Al plastic film. The prepared Cu foil, DAP–Cu current collector, and LFP-coated Al foil are cut into 2×2 cm^2 square electrode. The cut Cu foil is connected to the nickel tab using a welder, and the DAP–Cu electrode is placed on the surface of the Cu foil. The Al foil is connected to the Al tab, and the pre-deposited Li/DAP–Cu composite andoe is placed on one side of the Cu foil to serve as the anode. The LFP-coated Al foil serves as the cathode. The Celgard 2400 separator is used to separate the anode and cathode, which are then placed into the Al plastic flim for sealing. An appropriate amount of electrolyte is added, and the DAP–Cu and LFP are connected to the external circuit through the Cu foil and Al foil with its weld tabs, respectively.The N/P ratio of the DAP–Cu anode to the LiFePO$_4$ cathode is 1.2:1. This homemade

Batteries & Supercaps

Research Article
doi.org/10.1002/batt.202400304

Chemistry Europe
European Chemical
Societies Publishing

pouch cell setup is assembled in our lab to develop practical Li metal batteries, with dimensions of $(0.03 \times 0.03 \times 0.002)$ m^3.

Conflict of Interests

The authors declare no conflict of interest.

Data Availability Statement

The data that support the findings of this study are available from the corresponding author upon reasonable request.

[1] a) L. H. Li, Y. Zhang, T. J. Zhou, K. C. Wang, C. Wang, T. Wang, L. W. Yuan, K. X. An, C. H. Zhou, G. N. Lü, *Nat. Commun.* **2022**, *13*, 5315; b) G. Lin, Y. N. Zhao, J. Y. Fu, D. Jing, *Science* **2023**, *380*, 699–700; c) C. Y. Zhao, S. H. Ju, Y. Xue, T. Ren, Y. Ji, X. Chen, *Carb. Neutrality* **2022**, *1*, 7.

[2] a) O. Omoyele, M. Hoffmann, M. Koivisto, M. Larrañeta, J. M. Weinand, J. Linßen, D. Stolten, *Renewable Sustainable Energy Rev.* **2024**, *189*, 113792; b) X. F. Fu, D. Shen, Y. Z. Ji, S. Y. Zhao, H. R. Yu, W. Dong, *J. Energy Storage* **2024**, *82*, 110557; c) X. Chang, Y. M. Zhao, B. H. Yuan, M. Fan, Q. H. Meng, Y. G. Guo, L. J. Wan, *Sci. China Chem.* **2024**, *67*, 43–66; d) T. Hu, Q. Wu, C. Wang, J. L. Chen, F. Su, Z. B. Chen, Y. Z. Wang, J. Y. Chen, Y. W. Ma, J. Zhao, *Nano Res.* **2024**, https://doi.org/10.1007/s12274-024-6588-3; e) J. Y. Chen, Y. Z. Wang, Z. N. Tian, J. Zhao, Y. W. Ma, H. N. Alshareef, *InfoMat* **2023**, *6*, e12485.

[3] a) J. B. Hou, K. Zhang, J. H. Xiao, Z. Q. Xu, W. J. Gao, X. Y. Gao, S. K. Zhou, Z. Z. Jiao, M. R. Yi, Y. H. Yin, Z. P. Wu, *Tungsten* **2022**, *4*, 356–369; b) H. R. Cheng, Z. Ma, P. Kumar, H. H. Liang, Z. Cao, H. L. Xie, L. Cavallo, Q. Li, J. Ming, *ACS Energy Lett.* **2024**, *9*, 1604–1616; c) J. X. Wang, J. Ma, Z. F. Zhuang, Z. Liang, K. Jia, G. J. Ji, G. M. Zhou, H. M. Cheng, *Chem. Rev.* **2024**, *124*, 2839–2887; d) S. L. He, X. Shen, M. Han, Y. S. Liao, L. F. Xu, N. Yang, Y. M. Guo, B. C. Li, J. Shen, C. Zha, Y. L. Li, M. Wang, L. Wang, Y. F. Su, F. Wu, *ACS Nano* **2024**, *18(17)*, 11375–11388 https://doi.org/10.1021/acsnano.4c01263; e) Z. Y. Zhang, S. Said, A. J. Lovett, R. Jervis, P. R. Shearing, D. J. L. Brett, T. S. Miller, *ACS Nano* **2024**, *18*, 9389–9402; f) N. Yuan, Y. R. Deng, S. H. Wang, L. Gao, J. L. Yang, N. C. Zou, B. X. Liu, J. Q. Zhang, R. P. Liu, L. Zhang, *Tungsten* **2022**, *4*, 269–283; g) X. L. Zhao, M. Yang, Y. Wang, D. Wang, *Chem. Res. Chin. Univ.* **2023**, *39*, 630–635.

[4] a) Y. K. Xiao, X. X. Chen, J. H. Jian, Y. Cheng, Y. Zou, Y. Su, Q. L. Wu, C. Tang, Z. R. Zhang, M. S. Wang, J. M. Zheng, Y. Yang, *Small* **2024**, *20*, 2308472; b) H. Cui, Y. Z. Song, D. S. Ren, L. Wang, X. M. He, *Joule* **2024**,
8, 29–44; c) W. Wu, A. X. Wang, Q. S. Zhan, Z. L. Hu, W. J. Tang, L. Zhang, J. Y. Luo, *Small* **2023**, *19*, 2301737; d) Y. Z. Wang, C. Liu, J. Y. Chen, T. C. Guo, Z. N. Tian, Z. M. Zhao, Y. P. Zhu, X. X. Zhang, J. Zhao, Y. W. Ma, H. N. Alshareef, *Mater. Today Energy* **2024**, *40*, 101509; e) S. C. Wang, C. W. Qu, J. W. Wen, C. X. Wang, X. L. Ma, Y. Yang, G. Y. Huang, H. Y. Sun, S. M. Xu, *Mater. Chem. Front.* **2023**, *7*, 2779–2808.

[5] a) F. L. Tan, J. Yang, C. Zhou, *J. Cleaner Prod.* **2024**, *449*, 141574; b) Y. D. Lei, Z. L. Wang, D. Y. Wang, X. Y. Zhang, H. Z. Che, X. Yue, C. G. Tian, J. T. Zhong, L. F. Guo, L. Li, H. Zhou, L. Liu, Y. Y. Xu, *Nat. Clim. Change* **2023**, *13*, 693–700; c) K. J. Li, Y. Zhou, X. H. Huang, H. J. Xiao, Y. L. Shan, *Environ. Sci. Pollut. Res. Int.* **2024**, *114*, 10213–10233.

[6] a) G. Z. Zhang, J. Chang, L. G. Wang, J. W. Li, C. Y. Wang, R. Wang, G. L. Shi, K. Yu, W. Huang, H. H. Zheng, T. P. Wu, Y. H. Deng, J. Lu, *Nat. Commun.* **2023**, *14*, 1081; b) K. Y. Peng, P. Tang, Q. Q. Yao, Q. Y. Dou, X. B. Yan, *Nano Res.* **2023**, *16*, 9530–9537; c) H. Y. Wang, J. Wei, J. Y. Wang, D. Wang, *Chem. Res. Chin. Univ.* **2024**, *40*, 428–436 https://doi.org/10.1007/s40242-024-4062-0; d) J. Y. Chen, X. Xu, Q. He, Y. W. Ma, *Chem. Res. Chin. Univ.* **2020**, *36*, 386–401; e) G. R. Zheng, S. D. Xue, Y. H. Li, S. M. Chen, J. M. Qiu, Y. C. Ji, M. Liu, L. Y. Yang, *Nano Energy* **2024**, *125*, 109617; f) C. F. Li, J. Q. Wang, Q. Ye, P. Z. Li, K. Zhang, J. X. Li, Y. N. Zhang, L. Ye, T. B. Song, Y. Gao, B. J. Wang, H. S. Peng, *Small* **2024**, 2400570, https://doi.org/10.1002/smll.202400570; g) Y. L. An, Y. X. Zeng, D. Y. Luan, X. W. Lou, *Matter* **2024**, *7*, 1466–1502; h) J. Y. Chen, X. Qiao, W. Fu, X. R. Han, Q. Wu, Y. Z. Wang, Y. Zhang, L. Shi, J. Zhao, Y. W. Ma, *SmartMat.* **2023**, *4*, e1174; i) L. B. Song, R. H. Li, H. T. Zhu, Z. D. Li, G. Z. Liu, Z. Peng, X. L. Fan, X. Y. Yao, *Adv. Mater.* **2024**, *36*, 2400165, https://doi.org/10.1002/adma.202400165; j) X. B. Cheng, R. Zhang, C. Z. Zhao, Q. Zhang, *Chem. Rev.* **2017**, *117*, 10403–10473; k) Y. S. Feng, Y. N. Li, P. Wang, Z. P. Guo, F. F. Cao, H. Ye, *Angew. Chem. Int. Ed.* **2023**, *62*, e202310132; l) J. Y. Wang, Y. Cui, D. Wang, *Adv. Mater.* **2019**, *31*, 1801993; m) S. Y. Liu, B. Q. Gu, Z. H. Chen, R. M. Zhan, X. C. Wang, R. K. Feng, Y. M. Sun, *J. Energy Chem.* **2024**, *91*, 484–500; n) Z. X. Guo, T. R. Wang, D. H. Wang, H. H. Xu, X. Y. Liu, Y. M. Dai, H. Yang, Y. H. Huang, W. Luo, *ACS Nano* **2023**, *17*, 14136–14143.

[7] a) Y. R. Zhong, Q. Wang, S. M. Bak, S. Hwang, Y. H. Du, H. L. Wang, *J. Am. Chem. Soc.* **2023**, *145*, 7390–7396; b) H. Q. Ji, Z. K. Wang, Y. W. Sun, Y. Zhou, S. J. Li, J. Q. Zhou, T. Qian, C. L. Yan, *Adv. Mater.* **2023**, *35*, 2208590; c) Y. R. Zhong, Q. W. Shi, C. Q. Zhu, Y. F. Zhang, J. S. Francisco, H. L. Wang, *J. Am. Chem. Soc.* **2021**, *143*, 13929–13936; d) W. Xu, R. Y. Bi, M. Yang, J. Y. Wang, R. B. Yu, D. Wang, *Nano Res.* **2023**, *16*, 12745–12752; e) Y. Rao, J. W. Yang, S. Y. Chu, S. H. Guo, H. S. Zhou, *SmartMat* **2023**, *4*, e1205; f) T. Z. Li, X. W. Peng, P. Cui, G. Shi, W. Yang, Z. H. Chen, Y. F. Huang, Y. K. Chen, J. Y. Peng, R. Zou, X. Y. Zeng, J. Yu, J. J. Gan, Z. Y. Mu, Y. L. Chen, J. M. Zeng, J. Liu, Y. Y. Yang, Y. J. Wei, J. Lu, *SmartMat* **2021**, *2*, 519–553; g) R. Zhang, X. Chen, X. Shen, X. Q. Zhang, X. R. Chen, X. B. Cheng, C. Yan, C. Z. Zhao, Q. Zhang, *Joule* **2018**, *2*, 764–777.

[8] a) S. M. Chai, Y. Zhong, Y. J. Wang, Q. He, A. Azizi, L. Y. Chen, X. T. Ren, W. F. Wei, S. Q. Liang, Z. Chang, A. Q. Pan, *Adv. Energy Mater.* **2024**, *14*, 2303020; b) X. Y. Ni, J. Q. Zhou, K. C. Long, P. Qing, T. Y. Naren, S. Z. Huang, W. Liu, Q. W. Zhao, Y. J. Qian, T. Qian, C. L. Yan, L. B. Chen, *Energy Storage Mater.* **2024**, *67*, 103295; c) C. Wang, W. Z. Li, Y. H. Jin, J. B. Liu, H. Wang, Q. Q. Zhang, *Small* **2023**, *19*, 2300023; d) H. Su, Z. F. Chen, M. J. Li, P. X. Bai, Y. Li, X. Ji, Z. Q. Liu, J. Sun, J. Ding, M. Yang, X. Y. Yao, C. Mao, Y. H. Xu, *Adv. Mater.* **2023**, *35*, 2301171; e) S. J. Li, J. Y. Chen, G. Y. Liu, H. B. Wu, H. R. Chen, M. S. Li, L. Shi, Y. Z. Wang, Y. W. Ma, J. Zhao, *ACS Appl. Mater. Interfaces* **2022**, *14*, 56697–56706; f) J. Y. Chen, Y. Z. Wang, X. Qiao, J. Zhao, Y. W. Ma, H. N. Alshareef, *Adv. Sci.* **2022**, *10*, 2205695.

[9] a) J. L. Liu, T. Kaneko, J. Y. Ock, S. Kondou, K. Ueno, K. Dokko, K. Sodeyama, M. Watanabe, *J. Phys. Chem. C* **2023**, *127*, 5689–5701; b) T. T. K. Ingber, M. M. Bela, F. Püttmann, J. F. Dohmann, P. Bieker, M. Börner, M. Winter M C Stan, *J. Mater. Chem. A* **2023**, *11*, 17828–17840; c) Y. C. Liu, Z. C. Song, Z. H. Wang, J. X. Xing, W. Zou, J. Z. Li, *Mater. Chem. Front.* **2023**, *7*, 117–127; d) T. C. Cao, X. P. Cheng, M. M. Wang, J. X. Lu, J. J. Niu, H. Liu, X. Q. Liu, Y. F. Zhang, *ACS Appl. Mater. Interfaces* **2023**, *15*, 6666–6675; e) H. L. Fan, S. Wang, J. Y. Dong, W. C. Gao, Y. X. Liu, *J. Porous Mater.* **2023**, *30*, 1653–1661.

[10] a) Y. S. Ye, R. Xu, W. X. Huang, H. Y. Ai, W. B. Zhang, J. O. Affeld, A. Cui, F. Liu, X. Gao, Z. Y. Chen, T. Li, X. Xiao, Z. W. Zhang, Y. C. Peng, R. A. Vila, Y. C. Wu, S. T. Oyakhire, H. Kuwajima, Y. Suzuki, R. Matsumoto, Y. Masuda, T. Yuuki, Y. Nakayama, Y. Cui, *Nat. Energy* **2024**, https://doi.org/10.1038/s41560-024-01473-2; b) Q. Kang, Z. C. Zhuang, Y. J. Liu, Z. H. Liu, Y. Li, B. Sun, F. Pei, H. Zhu, H. F. Li, P. Li, Y. Lin, K. M. Shi, Y. K. Zhu, J. Chen, C. Q. Shi, Y. Zhao, P. K. Jiang, Y. Y. Xia, D. S. Wang, X. Y. Huang, *Adv. Mater.* **2023**, *35*, 2303460; c) G. X. Lu, J. W. Nai, D. Y. Luan, X. Y. Tao,

X. W. (David) Lou, *Sci. Adv.* **2023**, *9*, eadf1550; d) X. X. Peng, Q. S. Tu, Y. Q. Zhang, K. Jun, F. Y. Shen, T. Ogunfunmi, Y. Z. Sun, M. C. Tucker, G. Ceder, M. C. Scott, *Sci. Adv.* **2023**, *9*, eabq3285; e) J. F. Ding, R. Xu, Y. Xiao, S. Zhang, T. L. Song, C. Yan, J. Q. Huang, *Adv. Energy Mater.* **2023**, *13*, 2204305; f) Z. B. Zhang, J. Wang, H. Z. Qin, B. Zhang, H. Z. Lin, W. T. Zheng, D. Wang, X. B. Ji, X. Ou, *ACS Nano* **2024**, *18*, 2250–2260; g) L. D. Zhou, N. Minafra, W. G. Zeier, L. F. Nazar, *Acc. Chem. Res.* **2021**, *54*, 2717–2728; h) J. J. Xu, J. X. Zhang, T. P. Pollard, Q. D. Li, S. Tan, S. Hou, H. L. Wan, F. Chen, H. X. He, E. Y. Hu, K. Xu, X. Q. Yang, O. Borodin, C. S. Wang, *Nature* **2023**, *614*, 694–700; i) Y. S. Mwng, V. Srinivasan, K. Xu, *Science* **2022**, *378*, eabq3750.

[11] a) S. Li, S. J. Yang, G. X. Liu, J. K. Hu, Y. L. Liao, X. L. Wang, R. Wen, H. Yuan, J. Q. Huang, Q. Zhang, *Adv. Mater.* **2024**, *36*, 2307768; b) S. Zhang, J. F. Ding, R. Xu, Y. Xiao, C. Yan, J. Q. Huang, *Adv. Energy Mater.* **2024**, *14*, 2303726; c) J. Y. Chen, X. Qiao, X. R. Han, J. H. Zhang, H. B. Wu, Q. He, Z. B. Chen, L. Shi, Y. Z. Wang, Y. N. Xie, Y. W. Ma, J. Zhao, *Nano Energy* **2022**, *103*, 107814; d) L. Zeng, J. He, C. Y. Yang, D. Luo, H. B. Yu, H. N. He, C. H. Zhang, *Energy Storage Mater.* **2023**, *54*, 469–477; e) Z. Y. Ning, G. C. Li, D. L. R. Melvin, Y. Chen, J. F. Bu, D. S. Jolly, J. L. Liu, B. K. Hu, X. W. Gao, J. Perera, C. Gong, S. D. Pu, S. M. Zhang, B. Y. Liu, G. O. Hartley, A. J. Bodey, R. I. Todd, P. S. Grant, D. E. J. Armstrong, T. J. Marrow, C. W. Monroe, P. G. Bruce, *Nature* **2023**, *618*, 287–293.

[12] a) P. Bai, J. Li, F. R. Brushetta, M. Z. Bazan, *Energy Environ. Sci.* **2016**, *9*, 3221–3229; b) Z. Y. Lu, Y. Guo, S. W. Zhang, S. C. Wu, R. W. Meng, S. Hong, J. X. Li, H. Y. Xue, B. Y. Zhang, D. H. Fan, Y. F. Zhang, C. Zhang, W. Lv, Q. H. Yang, *Adv. Mater.* **2021**, *33*, 2101745.

[13] K. Romanenko, N. Avdievich, A. Wong, M. Gauthier, R. Pongilat, A. Jerschow, *Chem. Mater.* **2023**, *35*, 9789–9798.

[14] a) X. He, K. Zhang, Z. Q. Zhu, Z. F. Tong, X. Liang, *Chem. Soc. Rev.* **2024**, *53*, 9–24; b) J. Y. Zhou, J. Qin, H. Zhan, *ChemPhysChem* **2024**, *25*, e202400007, https://doi.org/10.1002/cphc.202400007; c) K. N. Zhong, X. Y. Hou, Y. H. Xue, W. L. Huang, B. C. Meng, L. J. Zhou, Z. Fang, L. B. Li, *J. Colloid Interface Sci.* **2024**, *653*, 697–706; d) X. G. Fei, H. Gao, Y. Z. Xu, W. S. Ma, B. Yu, F. Q. Tan, G. H. Cheng, Z. H. Zhang, *Energy Storage Mater.* **2024**, *65*, 103079; e) J. Y. Chen, G. Y. Liu, X. R. Han, H. B. Wu, T. Hu, Y. H. Huang, S. H. Zhang, Y. Z. Wang, Z. X. Shi, Y. Zhang, L. Shi, Y. W. Ma, H. N. Alshareef, J. Zhao. *ACS Nano.* **2024**, *18(21)*, DOI: 10.1021/acsnano.4c00720.

[15] a) G. D. Guo, K. Zhang, K. P. Zhu, P. Yang, Z. P. Shao, S. Z. Liu, L. Lin, W. B. Zhuang, P. Xue, Q. C. Zhang, Y. G. Yao, *Adv. Funct. Mater.* **2024**, 2402490, https://doi.org/10.1002/adfm.202402490; b) X. Ma, Z. J. Zhang, J. M. Wang, S. H. Sun, S. F. Zhang, S. Yuan, Z. J. Qiao, Z. Y. Yu, J. L. Kang, W. J. Li, *Rare Met.* **2021**, *40*, 2802–2809; c) J. M. Wang, Z. J. Zhang, S. H. Sun, S. Yuan, W. J. Li, Z. J. Qiao, Z. Y. Yu, J. L. Kang, *Surf Innov.* **2021**, *9*, 207–213; d) W. B. Liu, B. B. Lu, X. J. Liu, Y. Gan, S. C. Zhang, S. Q. Shi, *Adv. Funct. Mater.* **2021**, *31*, 2101999; e) Y. P. Tang, K. Shen, Z. Y. Lv, X. Xu, G. Y. Hou, H. Z. Cao, L. K. Wu, G. Q. Zheng, Y. D. Deng, *J. Power Sources* **2018**, *403*, 82–89.

[16] C. P. Yang, Y. X. Yin, S. F. Zhang, N. W. Li, Y. G. Guo, *Nat. Commun.* **2015**, *6*, 8058.

[17] S. H. Wang, Y. X. Yin, T. T. Zuo, W. Dong, J. Y. Li, J. L. Shi, C. H. Zhang, N. W. Li, C. J. Li, Y. G. Guo, *Adv. Mater.* **2017**, *29*, 1703729.

[18] a) J. Y. Chen, S. J. Li, X. Qiao, Y. Z. Wang, L. N. Lei, Z. Y. Lyu, J. Zhao, Y. Zhang, R. Q. Liu, Q. H. Liang, Y. W. Ma, *Small* **2022**, *18*, 2105999; b) A. G. Jia, J. M. Chao, C. Qin, X. T. Guo, G. Q. Yuan, J. J. Liu, H. Pang, *Chem. Eng. J.* **2024**, *408*, 148103; c) G. D. Yang, Y. Liu, X. Ji, S. M. Zhou, Z. Wang, H. Z. Sun, *Chem. Eur. J.* **2024**, *30*, e202304152; d) Y. H. Liu, Y. F. Li, Z. Z. Du, C. He, J. X. Bi, S. Y. Li, W. Q. Guan, H. F. Du, W. Ai, *Adv. Sci.* **2023**, *10*, 2301288; e) N. L. Shen, H. Liu, W. B. Tang, Z. C. Liu, T. Wang, Y. Ma, Y. R. Zhong, J. R. He, Z. Zhu, Y. P. Wu, X. B. Cheng, *Ind. Eng. Chem. Res.* **2023**, *62*, 15360–15377; f) C. Zhang, R. Y. Lyu, W. Lv, H. Li, W. Jiang, J. Li, S. C. Gu, G. M. Zhou, Z. J. Huang, Y. B. Zhang, J. Q. Wu, Q. H. Yang, F. Y. Kang, *Adv. Mater.* **2019**, *31*, 1904991.

[19] J. Y. Chen, J. Zhao, L. N. Lei, P. Li, J. Chen, Y. Zhang, Y. Z. Wang, Y. W. Ma, D. Wang, *Nano Lett.* **2020**, *20*, 3403–3410.

[20] a) W. Lu, Z. Wang, G. R. Sun, S, M. Zhang, L. N. Cong, L. Lin, S. R. Chen, J. Liu, H. M. Xie, Y. L. Liu, *J. Energy Chem.* **2023**, *80*, 32–39; b) J. L. Jiang, X. F. Hu, S. Y. Lu, C. Shen, S. S. Huang, X. Y. Liu, Y. Jiang, J. J. Zhang, B. Zhao, *Energy Storage Mater.* **2023**, *54*, 885–894; c) D. Luo, L. Zheng, Z. Zhang, M. Li, Z. W. Chen, R. G. Cui, Y. B. Shen, G. R. Li, R. F. Feng, S. J. Zhang, G. P. Jiang, L. W. Chen, A. P. Yu, X. Wang, *Nat. Commun.* **2021**, *12*, 186; d) W. Yu, J. L. Yang, J. Li, K. Zhang, H. M. Xu, X. Zhou, W. Chen, K. P. Loh, *Adv. Mater.* **2021**, *33*, 2102083.

[21] a) S. Pyo, S. Ryu, Y. J. Gong, J. Cho, H. Yun, H. Kim, J. Lee, B. Min, Y. Choi, J. Yoo, Y. S. Kim, *Adv. Energy Mater.* **2023**, *13*, 2203573; b) S. B. Huang, L. Chen, T. S. Wang, J. K. Hu, Q. F. Zhang, H. Zhang, C. W. Nan, L. Z. Fan, *Nano Lett.* **2021**, *21*, 791–797; c) J. W. Liu, J. L. Jiang, Q. Y. Zhou, Z. H. Chen, R. H. Zhang, X. F. Xu, X. Han, S. H. Yang, Z. Zhou, P. Cheng, W. Shi, *eScience* **2023**, *3*, 100094; d) W. Y. Guan, Y. Lv, C. Ma, Q. X. Zhang, A. Wei, X. Z. Liu, *Mater. Chem. Front.* **2023**, *7*, 315–324; e) G. T. Yu, S. H. Chung, *Small* **2023**, *19*, 2303490; f) X. L. Zhang, L. Ma, Y. P. Cai, J. Fransaer, Q. F. Zheng, *Matter* **2024**, *7*, 583–602.

[22] a) Y. Chang, M. L. Lye, H. C. Zeng, *Langmuir* **2005**, *21*, 3746–3748; b) J. Y. Chen, W. X. Zhou, J. Chen, Y. Fan, Z. Q. Zhang, Z. D. Huang, X. M. Feng, B. X. Mi, Y. W. Ma, W. Huang, *Nano Res.* **2015**, *8*, 1017–1025; c) J. Y. Chen, J. Chen, Y. Li, W. X. Zhou, X. M. Feng, Q. L. Huang, J. G. Zheng, R. Q. Liu, Y. W. Ma, W. Huang, *Nanoscale* **2015**, *7*, 16874–16879.